J. Fluid Mech. (1998), *vol.* 368, *pp.* 27–50. Printed in the United Kingdom

Secondary instability in rotating channel flow

By M. MATSUBARA AND P. H. ALFREDSSON

Department of Mechanics, Royal Institute of Technology, S-100 44, Stockholm, Sweden

(Received March 14 1997 and in revised form 12 January 1998)

Experiments on rotating channel flow, where both the primary (induced by a Coriolis instability) and the secondary instability are triggered independently, are described, focusing on the development of a secondary instability consisting of high-frequency travelling waves and their subsequent breakdown. Detailed hot-wire velocity measurements of the secondary disturbance are made and the phase speed and growth rate for various frequencies are determined. It is shown that the frequency of highest growth rate is close to that which is observed for naturally developing flow. Some information on the later stages in the transition process is obtained from frequency spectra, which show that interaction between various modes gives rise to stochastic low-frequency disturbances, which may play an important role in the transition process. A theoretical model of the disturbance structure is described which is used to explain some of the measured results and also allows the determination of the disturbance cross-stream flow field from only streamwise velocity measurements.

1. Introduction

A classical scenario of transition to turbulence consists of growth of a primary instability followed by a secondary instability, which gives rise to further nonlinear interactions towards a complicated or chaotic state which develops into turbulence. The primary instability is in most cases well understood and can, in the linear stage, be described by classical hydrodynamic stability theory. In flows where the primary instability consists of stationary roll cell disturbances (such as the Taylor–Couette, curved or rotating channel flow) the secondary instability can take the form of streamwise travelling waves. On the other hand in flat-plate boundary layer transition, where the primary instability consists of two-dimensional Tollmien–Schlichting (TS) waves, the secondary instability manifests itself through the development of three-dimensionality of the TS-waves. Klebanoff, Sargent & Tidstrom (1962) controlled the three-dimensionality by attaching regularly distributed roughness elements in the spanwise direction which led to the so-called K-breakdown scenario. Later experiments have used one two-dimensional wave and a pair of oblique waves to study both K-breakdown and subharmonic breakdown under controlled conditions (see for instance Corke & Mangano 1988).

However for travelling wave type secondary instability developing on a stationary primary disturbance no physical experiment has been performed where the time-dependent secondary instability has been triggered in a controlled manner (except for a few results presented by Swearingen & Blackwelder 1987 for Görtler flow). In direct numerical simulations (DNS) on the other hand this type of secondary instability has been analysed by introducing a small disturbance of a certain wavelength and studying its development, see for instance Finlay (1990).

1.1. *Observation of secondary instability in curved or rotating boundary layer flows*

One of the first studies to investigate the interaction of steady streamwise vortices with travelling waves was made by Tani & Aihara (1969) who investigated the development of Görtler vortices on a concave wall together with the generation of two-dimensional TS-waves (for a recent review of Görtler vortices see Saric 1994). Although this investigation was not very detailed they found that breakdown to turbulence occurred first where the boundary layer was thickest, i.e. in the upwash region where the flow velocity was low. Bippes & Görtler (1972) also did experiments on flow along a concave wall using both flow visualization and hot-wire anemometry. They detected a wavy type of instability with a streamwise wavelength of the order of the spanwise scale of the original streamwise vortices. Hot-wire traces showed regular sinusoidal fluctuations in the region of the wavy motion.

Flow visualization studies by Aihara & Koyama (1981) and later Swearingen & Blackwelder (1987) showed the existence of another type of disturbance in the form of horseshoe type vortices. The two types of instability, i.e. wavy and horseshoe, will in the following be denoted sinuous (out-of-phase) and varicose (in-phase), respectively.

Masuda, Hori & Matsubara (1995) showed that in a boundary layer developing along a rotating flat plate, longitudinal vortices due to a Coriolis instability form and that these vortices are similar to Görtler vortices. They also visualized naturally occurring secondary instability and observed the two different types of secondary instability discussed above. By triggering the spanwise wavelength with roughness elements they showed that a large spanwise wavelength of the primary instability resulted in the varicose secondary instability, whereas a small wavelength was associated with the sinuous mode. This is also in accordance with results for curved boundary layer flow by Li & Malik (1995), who used the PSE-formulation to solve for the basic flow field as well as to carry out the stability analysis. They confirmed the experimental results of Masuda *et al.* that the mode type selection depends on the wavelength of the Görtler vortices.

There has been a number of other recent theoretical/numerical investigations of secondary instability in Görtler flow. Yu & Liu (1991) carried out a linear analysis of travelling waves, based on a nonlinear (streamwise independent) calculation of the primary instability. The flow parameters as well as the spanwise wavelength were chosen from the experiments by Swearingen & Blackwelder (1987). In the analysis the cross-flow velocities were neglected and only the streamwise mean velocity field was taken into account. They found that both sinuous and varicose modes were growing although the former had the largest growth rate. Both the streamwise wavelength and amplitude distribution were found to be in good agreement with the results of Swearingen & Blackwelder (1987). It was also shown that the disturbance amplitudes were largest in regions of local inflectional profiles (for the varicose mode normal profiles at the upper part of the Görtler structure and for the sinuous mode the spanwise profiles at each side of the upwash region).

DNS results by Liu & Domaradzki (1993) of one vortex pair in Görtler flow, where the data of Swearingen & Blackwelder (1987) were used to set the amplitude of the primary instability, made them conclude that the spanwise shear was governing the onset of secondary instability. They also did a linear stability analysis which supports this conclusion (see also the paper by Bottaro & Klingmann 1996).

1.2. *Instability in rotating and curved channel flows*

In rotating channel flow the governing parameters are the Reynolds number ($Re = U_b d/\nu$, where U_b is the bulk velocity, d is the channel width and ν is the kinematic

viscosity of the fluid) and the rotation number ($Ro = \Omega d/U_b$, where Ω is the system angular velocity). For small values of Ro these parameters combine in such a way that the important parameter for the primary instability is $Re\,Ro^{1/2}$, which is similar to the Dean number in curved channel flow. The primary instability occurs when this parameter exceeds a critical value (Lezius & Johnston 1976; Alfredsson & Persson 1989). When the streamwise vortices grow, they make the flow field three-dimensional though the flow is still laminar. On top of the primary instability several types of secondary instability have been observed. They include merging and splitting of the primary vortex pairs, as well as streamwise travelling waves of two types, usually denoted undulating and twisting motions. The twisting motion has a shorter streamwise wavelength, of the same order as the spanwise wavelength of the primary instability, whereas the undulating motion typically has a wavelength which is an order of magnitude larger.

We should note that the instability in channel flows differs from that in boundary layers, since the Reynolds number is constant in the channel flow case whereas it increases in the downstream direction in the boundary layer case. In the boundary layer case the flow will ultimately reach the turbulent state, whereas in channel flow the disturbance level may saturate.

The stability of plane channel flow subjected to spanwise system rotation was first studied experimentally by Alfredsson & Persson (1989). They visualized the twisting secondary instability as well as the primary instability using reflective flakes in water. Their study also shows splitting and merging of the longitudinal vortices; however the twisting motion seems to be the most important element leading to turbulent flow. Yang & Kim (1991) confirmed many of the experimental results of Alfredsson & Persson through a DNS in a large computational domain where the disturbances could develop freely. The twisting motion arises spontaneously in the simulation at typical parameter values where they were also observed in experiments. They also observed a longer wavelength disturbance although the twisting motion had the largest growth rate. The twisting motion had a propagation speed of about $1.1U_b$.

For the rotating channel flow three types of secondary instability, splitting and merging of the longitudinal vortices, undulating and twisting motions, were also predicted numerically by Finlay (1990, 1992) and Guo & Finlay (1991). The splitting and merging were described as an Eckhaus instability, which would also play an important role in selecting the spanwise wavelength of streamwise vortices, and comparison with the data obtained by Alfredsson & Persson (1989) seemed to verify these results. For the twisting motion, corresponding to that observed by Alfredsson & Persson, the maximum growth rate was obtained for a streamwise wavelength of $1.5d$. The wave speed was about $1.15U_b$. For high Reynolds numbers modulation of the twisting motion was observed leading to chaotic behaviour and finally to turbulent flow (Finlay, 1992).

As indicated above there is a strong similarity between the flow in a curved channel and in a rotating channel and so far there exist more experimental results for curved channel flow. For instance the spatial development of the primary instability as well as twisting and undulating motions have been studied by Matsson & Alfredsson (1990, 1992, 1994). However only naturally occurring secondary instabilities were studied and a mixture of the undulating and twisting motion was observed. Since the frequencies of these two motions differ by an order of magnitude the two instabilities were sorted through band-pass filtering of the measured velocity signals. The results indicate that both the twisting and undulating secondary instabilities are related to the low-velocity region between a vortex pair at the concave wall where the mean flow

is strongly inflectional. Also, in the numerical simulation of curved channel flow by Finlay, Keller & Ferziger (1988) both undulating and twisting motions were observed. Linear stability analysis by Le Cunff & Bottaro (1993) who analysed the stability properties of spanwise profiles obtained from numerical simulations showed that at low Reynolds numbers only the sinuous mode was unstable whereas at high Re the varicose mode could also become unstable.

1.3. *Outline*

In the present paper we will describe experiments in a rotating channel flow where both the primary and secondary instability are triggered independently. We focus on high-frequency disturbances and their breakdown. The experiments use hot-wire anemometry to measure the time-dependent velocity field and the disturbances are described in detail, regarding their spatial structure, growth rate and propagation speed. Information of the later stages in the transition process is obtained from frequency spectra of the streamwise velocity signal. It is shown that interactions between various modes give rise to stochastic low-frequency disturbances which probably are an important ingredient in the transition scenario. The paper is organised as follows: §2 describes the experimental apparatus and measurement techniques, §3 contains the experimental results whereas §4 describes a theoretical model which is used to explain some of the measured results but also allows us to estimate the cross-stream flow field from only streamwise velocity measurements. These results are also compared with previous DNS results and good agreement is obtained.

In many wall-bounded shear flows transition to turbulence has as a precursor the development of streamwise oriented regions of high and low velocity and turbulence breakdown is often due to the development of high-frequency (short-wavelength) travelling waves on these structures. The present results may hence have a wider applicability than just to describe transition in rotating channel flow.

2. Experimental set-up

2.1. *Rotating channel and velocity measurement*

The experiments were carried out in a straight channel on a rotating table (see figure 1), previously used by Matsubara & Alfredsson (1996). A stationary air supply consisting of a fan, a flow rate orifice meter and a 80 dm^3 damping chamber distributed air to the rotating system via a mechanical rotating seal. A perforated pipe distributed the air into the settling chamber where two screens are mounted upstream of a 24:1 contraction. The 1 m long test channel has a width of 10 mm and a height of 290 mm giving a 29:1 aspect ratio. A fine mesh at the downstream end of the channel reduces upstream influence when the air leaves the channel during rotation. For flow noise reduction, a muffler was installed before the settling chamber.

An automatic traversing mechanism enabled remote controlled measurement where the hot wire(s) could be traversed in the wall-normal direction y and the spanwise direction z. In the streamwise direction x the traversing mechanism was manually moved. The rotating and the stationary systems were connected through a 12-channel carbon slip ring device and a 4-channel mercury rotating coupling, which were utilized for measurement signals and electronic power supply, respectively. The in-house built hot-wire anemometer was placed on the rotating table and had 10 times amplification for DC output and 100 times for AC output. These large amplification rates reduce the influence of electronic noise from the slip rings and electronic devices and enabled

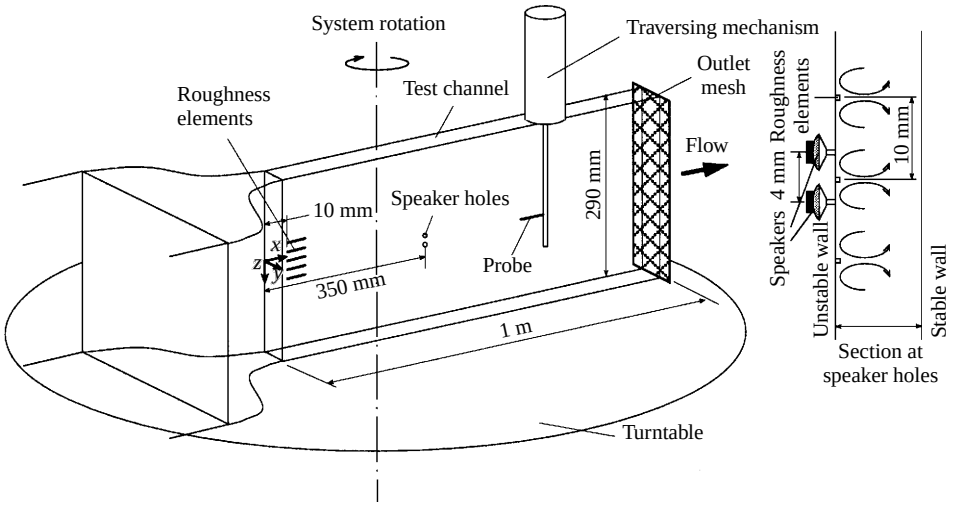

FIGURE 1. Experimental set-up.

high-resolution measurements of the velocity fluctuations. The hot wire had a length of 0.5 mm and a diameter of 2.5 μm.

The hot wire was calibrated against the fully developed parabolic profile in the downstream part of the channel. Some calibrations were also made by changing the velocity in the channel. Excellent agreement between the two methods was obtained.

2.2. *Initial disturbances*

In order to control primary and secondary instability two kinds of initial disturbance were introduced as shown in figure 1. The vortices of the primary instability were triggered by small roughness elements located at the unstable side close to the channel inlet. The roughness elements were 0.5 mm high and 2 mm wide and had a length of 18 mm. They were spaced regularly in the spanwise direction a distance of 10 mm apart that gives a non-dimensional spanwise wavenumber $\beta = 2\pi d/\lambda = 6.28$, where λ is the spanwise wavelength (10 mm). This spanwise wavelength was empirically chosen to minimize large-scale secondary instability such as undulation and splitting/merging that can make it difficult to observe the short-scale secondary instability.

For secondary instability, periodic injection and suction through two holes on the unstable wall at $x = 350$ mm were generated by small headphone speakers. The disturbances could be generated to be either out-of-phase or in-phase. The holes had a diameter of 1 mm and were separated by 4 mm in the spanwise direction. This distance is comparable with the spanwise size of the low-velocity region. The central roughness element was adjusted to be on the symmetry line between the holes so that the time-periodic disturbance is either symmetric or antisymmetric with respect to the centre of the upwash region. The intensity of the initial disturbance v_{init}/U_b was of the order of 1% evaluated from the r.m.s. of the velocity normal to the wall at the exit of the holes when measured with the hot wire without flow in the channel. An estimate of the initial disturbance can also be found in figure 2 where the disturbance 36 mm downstream of the generation point is shown for the out-of-phase case (without channel rotation). Though the amplitude of u is 0.01%, the disturbance is clearly antisymmetric in the spanwise direction and consists of inclined structures in the (y, t)-plane as shown in figure 2(*c*,*d*). Most of the results presented in the

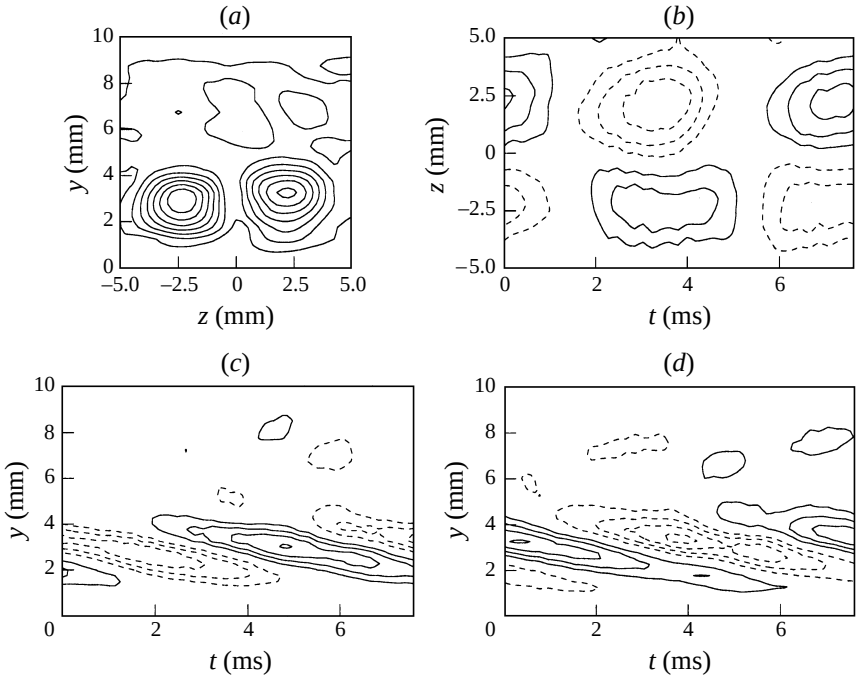

FIGURE 2. Initial disturbance at $x = 386$ mm with forcing frequency $F_1 = 131$ Hz: (*a*) r.m.s. of streamwise velocity in (y, z)-plane, (*b*) velocity disturbance in (z, t)-plane at $y = 3.3$ mm, (*c*) velocity disturbance in (y, t)-plane at $z = -2.5$ mm, (*d*) velocity disturbance in (y, t)-plane at $z = 2.5$ mm. Contour spacing is 0.002% U_b for (*a*) and 0.005% U_b for (*b*) (*c*) and (*d*). Negative contours are dashed.

following were obtained by using this amplitude of the initial disturbance; however when determining the growth rate of the secondary instability the initial amplitude was an order of magnitude smaller, in order to obtain a sufficiently long distance where the disturbance could be viewed as linear.

Control of the generation of the secondary instability, as well as of the traversing system and data sampling, was performed with a personal computer (Macintosh) and a AD/DA conversion board (National Instrument). Forcing frequencies were in the range 100–200 Hz and the signal from the DA output was amplified by a hi-fi stereo amplifier. Typically when measurements of both forced and unforced cases were made they were made sequentially, first with forcing and then without forcing before moving the probe. Without forcing the sampling duration was typically 2.3 s with 5.2 kHz sampling rate. In the case of a forced flow the sampling frequency was chosen such that there were 40 sampling points within each period of the forcing signal. Ensemble averages were formed from 300 periods of the signal and each y, z cross-section consisted of 18 points evenly spaced normal to the wall and 26 points (with increment 0.5 mm) in the spanwise direction (in total 468 measurement points).

2.3. *Choice of experimental parameters*

Observations of secondary instability in plane rotating channel flow were first made by Alfredsson & Persson (1989) through flow visualization in water. They found a short-wavelength travelling wave at $Re = 590$ and $Ro = 0.084$. The relevant parameter for the instability (for small rotation numbers) is $Re\,Ro^{1/2}$ which for their case was 170. In the present apparatus the maximum rotation rate is 1.2 s per revolution

and we chose $Re = 1300$ and $Ro = 0.026$ which gave $Re\,Ro^{1/2} = 210$. These values were chosen since it was the lowest Re for which it was possible to detect naturally occurring secondary disturbances at the end of the channel. All results in the following relate to the out-of-phase mode, since only this mode had a positive growth rate for the present case.

3. Results and discussion

3.1. *Basic flow*

The Coriolis force instability in a rotating channel flow gives rise to counter-rotating longitudinal vortices which interact with the pressure-driven Poiseuille flow. The primary vortices were triggered by small roughness elements which generate a small upwash flow from the unstable wall. This upwash flow develops into a pair of counter-rotating longitudinal vortices. Although the flow disturbance is quite small the large growth rate of this type of instability gives rise to large disturbances in the streamwise velocity further downstream. The general development of the primary disturbance without the influence of secondary instabilities shows first an exponential growth, then a smaller growth until a maximum level is reached after which the disturbance saturates at a lower level. Figure 3 shows contours of the time-averaged streamwise velocity from three different streamwise positions corresponding to the maximum level ($x = 436$ mm), and two positions in the saturated region. In the figure the parabolic profile has been subtracted and the disturbance velocity normalized with the bulk velocity U_b. Two different cases are shown: one in which only natural secondary instability occurs, the other in which out-of-phase secondary instability is triggered at $x = 350$ mm.

By $x = 436$ mm (figure 3*a*) the streamwise disturbance velocity reaches values larger than 50% of U_b. A prominent feature is the localized low-velocity region close to the unstable wall where the flow is rather symmetric around the centre of the low-velocity region ($z = 0$). At $x = 636$ mm the disturbance field is close to that at $x = 436$ mm although the large spanwise shear near both walls has decreased significantly. At $x = 836$ mm the most prominent feature is that the flow is no longer symmetric, probably due to the primary roll cells being affected by splitting or merging of neighbouring vortex pairs.

In the case of the forced flow the initial position is almost no different to the unforced case indicating that the initial disturbance at this stage can be regarded as linear. Even at $x = 636$ mm there are only small differences, mainly occurring in the low-velocity region where the forcing start to affect the mean flow, flattening the velocity distribution in the spanwise direction at the centre of the channel. Further downstream, at $x = 836$ mm, the mean flow is still symmetric unlike the asymmetric shape without forcing. This observation indicates that the deterministic forcing of the wavy motion prohibited the growth of another type of secondary instability (merging/splitting).

A useful way to show the amplitude development of a stationary disturbance is to evaluate the deviation from the undisturbed flow field. Matsson & Alfredsson (1992) introduced a measure e defined as

$$e = \left(\frac{1}{A U_b^2} \int \int_A (U - U_{parabolic})^2 \mathrm{d}A \right)^{1/2}. \tag{3.1}$$

Figure 4 shows the change of e in the streamwise direction for the cases with and

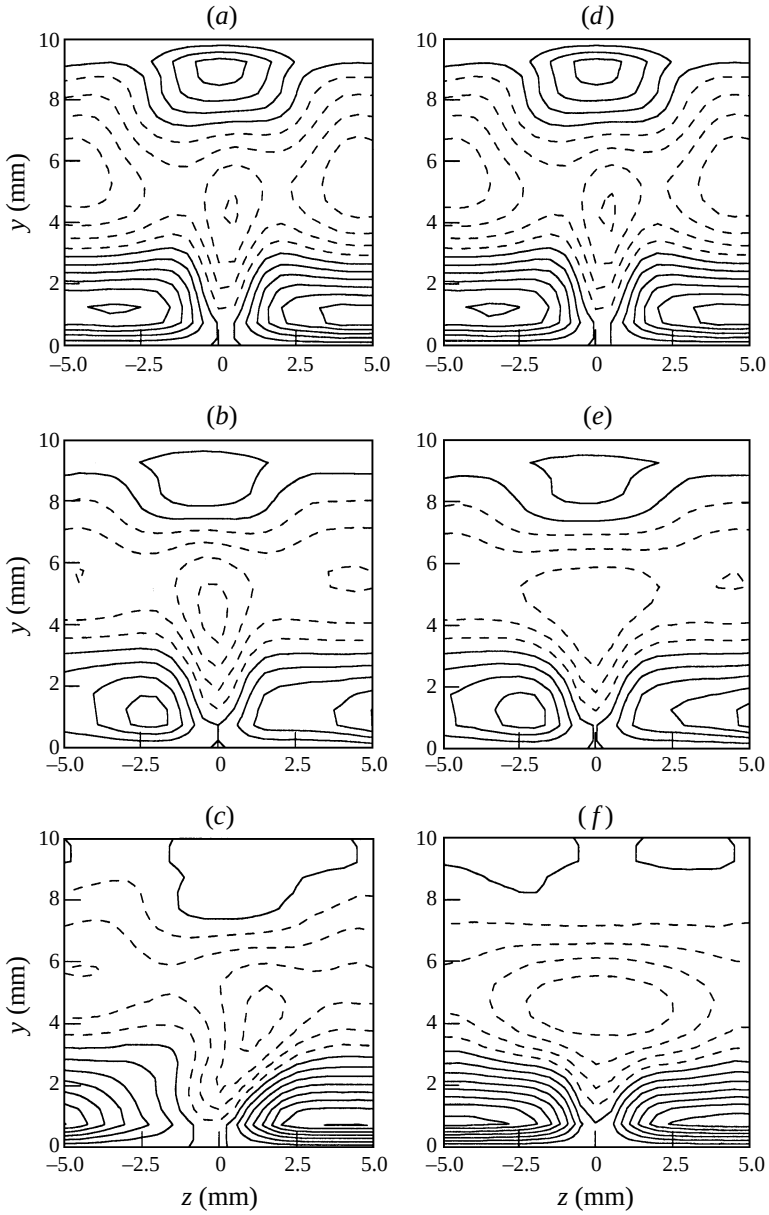

FIGURE 3. Time-averaged velocity field with parabolic profile subtracted. Without forcing: (*a*) $x = 436$ mm, (*b*) $x = 636$ mm (*c*) $x = 836$ mm, with forcing $F_1 = 131$ Hz: (*d*) $x = 436$ mm, (*e*) $x = 636$ mm, (*f*) $x = 836$ mm. Contour spacing is $0.10U_b$.

without forcing. The amplitude overshoots around 400 mm and is approximately constant from 486 mm to 686 mm. At 838 mm a sudden increase in e is seen in the case without forcing. This increase is related to the asymmetric appearance of the flow field seen in figure 3(*c*).

Matsson & Alfredsson (1994) found that in curved channel flow, naturally occurring twisting motion was only observed in the saturated region. In this paper the development of the secondary instability is therefore investigated in the region where

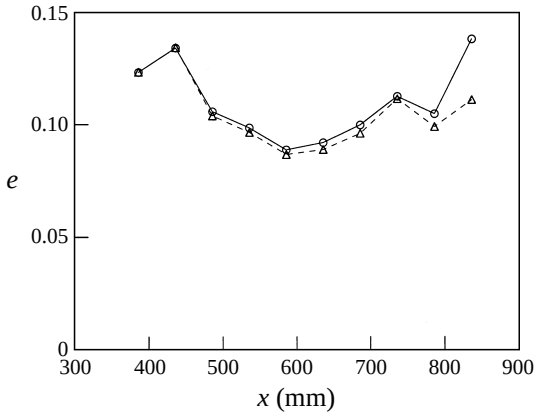

FIGURE 4. Streamwise development of the primary instability: ○, without forcing; △, with forcing; $F_1 = 131$ Hz.

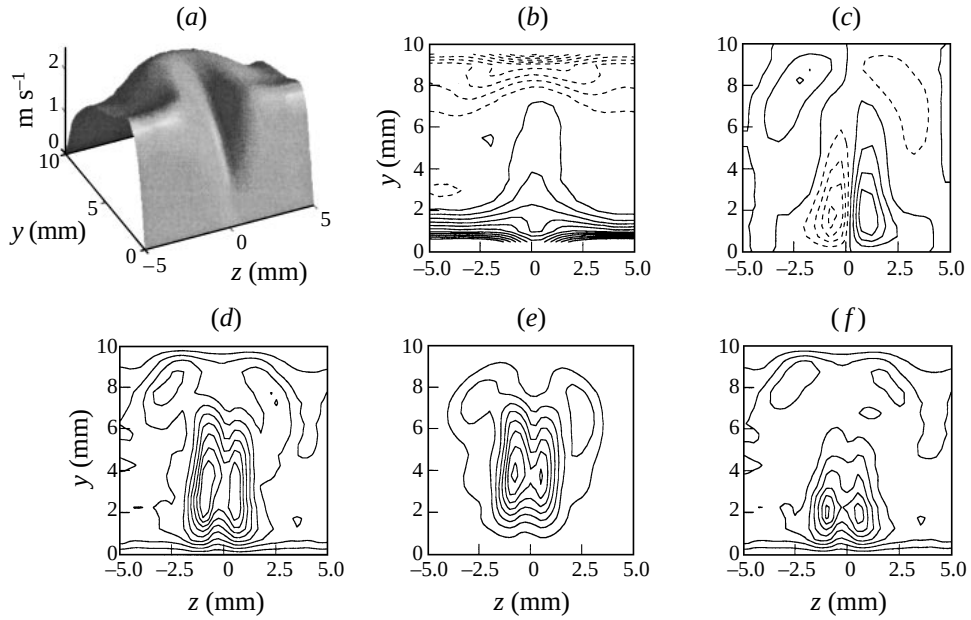

FIGURE 5. Relation between time-averaged flow field and secondary instability at $x = 436$ mm. (*a*) distribution of mean streamwise velocity, (*b*) wall-normal gradient of mean streamwise velocity, (*c*) spanwise gradient of mean streamwise velocity, (*d*) total r.m.s., (*e*) r.m.s. of streamwise velocity for fundamental and all harmonic modes, (*f*) r.m.s. of random motion. Contour spacing is $0.10U_b/d$ for (*b*) and (*c*) and 0.25% U_b for (*d*), (*e*) and (*f*).

the primary disturbance is close to saturated, i.e. where the mean flow is only changing slightly in the streamwise direction. The mean flow in the saturated region is called 'basic flow' for secondary instability in this paper.

3.2. *Structure of secondary instability*

Figure 5 shows a comparison between the basic flow field and the occurrence of secondary instability. The basic flow field is shown in figure 5(*a*) in a three-dimensional plot which emphasizes the narrow low-speed region and the constant-velocity region

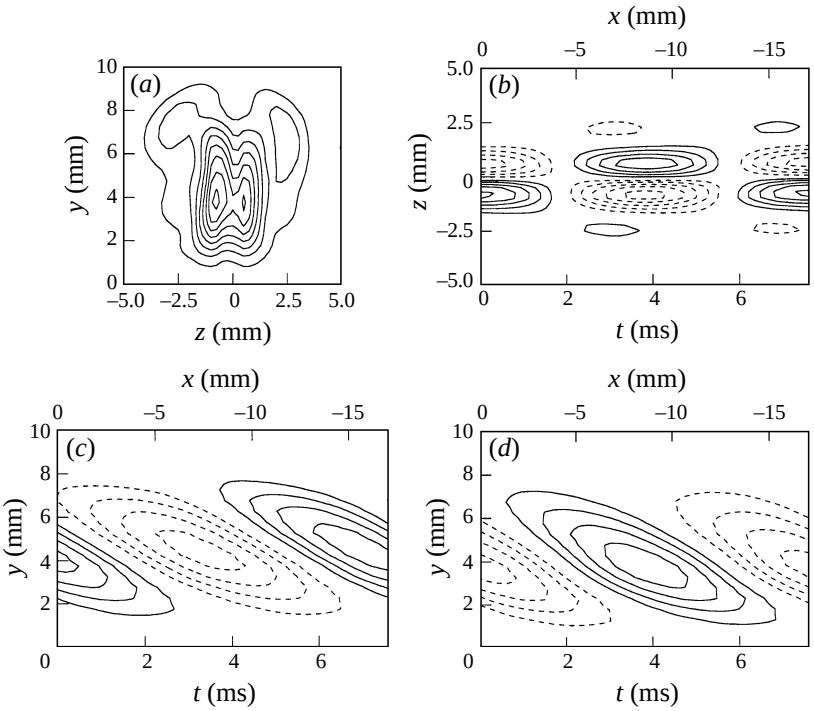

FIGURE 6. Structure of secondary instability at $x = 436$ mm: (*a*) r.m.s. of streamwise velocity, (*b*) velocity disturbance in (z,t)-plane at $y = 3.8$ mm, (*c*) velocity disturbance in (y,t)-plane at $z = -0.5$ mm, (*d*) velocity disturbance in (y,t)-plane at $z = 0.5$ mm. Contour spacing is 0.25% U_b for (*a*) and 0.5% U_b for (*b*) (*c*) and (*d*). Negative contours are dashed.

to its sides. The normal and spanwise velocity gradients are shown in figures 5(*b*) and 5(*c*), respectively. The r.m.s. of the fluctuating u-velocity is shown in figure 5(*d*) and clearly shows a two-peak distribution located in the region where strong gradients are apparent in the mean velocity distribution and it is seen that the disturbance is correlated to large values of the spanwise gradient rather than to the gradient normal to the wall. Figure 5(*e*) shows the r.m.s. of the fundamental mode and its harmonics, obtained from phase-averaged data whereas figure 5(*f*) shows the random contribution.

In order to show the structure of the secondary instability figures 6–8 show the time-resolved measurements at the three downstream positions for which the basic flow field previously was shown. All figures show (*a*) the (y,z)-plane of the r.m.s.-distribution of the disturbance, (*b*) a time resolved (z,t)-plane taken at $y = 3.75$ mm, whereas (*c*) and (*d*) show time resolved (y,t)-planes taken at $z = +0.5$ mm and $z = -0.5$ mm respectively. The t-axis in these plots was chosen such that its physical length is approximately the same as the abscissa when the propagation velocity of the disturbance is used to convert it to a length. In this way the figures give an almost correct picture of the physical extent and inclination of the disturbance. The initial disturbance was out of phase and this is clearly seen at 436 mm in figure 6(*b*), which shows a well ordered antisymmetric pattern of high- and low-velocity regions. The streamwise wavelength is approximately 17 mm, whereas the spanwise width of each region is of the order of 2 mm. In the (y,t)-plane it is seen that the structures are inclined in the streamwise direction with an angle of the order of 30°. In figure 6(*b–d*) the high- and low-velocity regions are similarly shaped with fore-and-aft symmetry

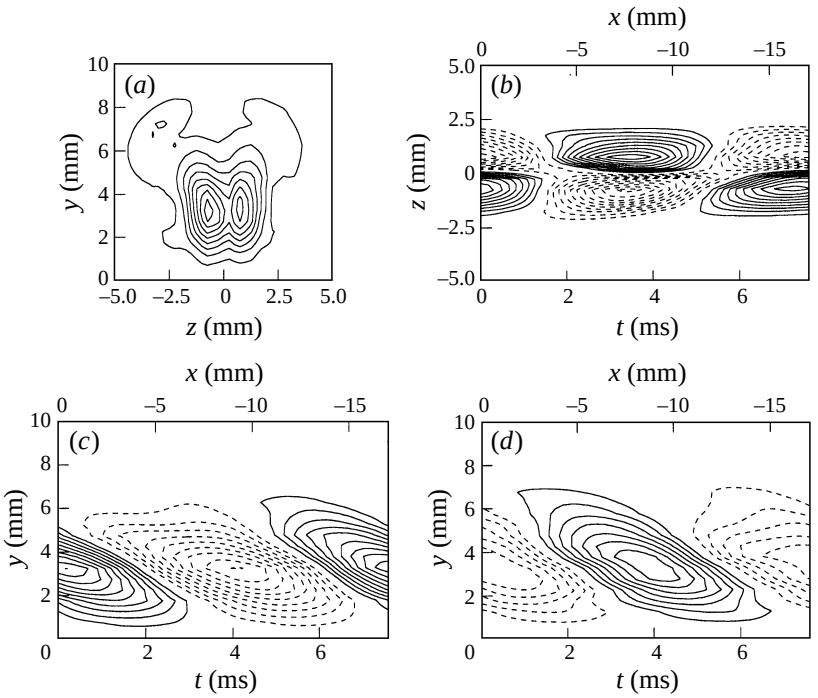

FIGURE 7. Structure of secondary instability at $x = 636$ mm: (*a*) r.m.s. of streamwise velocity, (*b*) velocity disturbance in (z,t)-plane at $y = 3.8$ mm, (*c*) velocity disturbance in (y,t)-plane at $z = -0.5$ mm, (*d*) velocity disturbance in (y,t)-plane at $z = 0.5$ mm. Contour spacing is 1% U_b.

which indicates that at this stage the secondary disturbance can still be viewed as linear.

Further downstream at $x = 636$ mm (figure 7) the disturbance structure is basically the same although the disturbance amplitude is an order of magnitude larger. The (z,t)-plane shows however a deformation of the structure where the leading edge (i.e. the left part of the structure) seems to spread from the centreline. At $x = 836$ mm (figure 8) the structure is less coherent since the influence of random modes starts to become important, and it also seems that there is a difference between the high- and low-speed regions which indicates that at this stage nonlinear effects starts to affect the coherent structure. The (z,t)-plane shows that the spanwise spreading of the structure continues, especially at the leading edge. The amplitude, however, has not increased compared to $x = 636$ mm but the position of the peaks is shifted towards the unstable wall.

During its downstream propagation the inclination of the structure with respect to the wall is also changed. The inclination of the structure was estimated by correlating the structure in the (y,t)-plane (at the z of maximum amplitude) with the function

$$\sin(\gamma y - \omega t)$$

and maximizing the correlation with γ as a variable. The angle of the inclination to the wall is then obtained as

$$\theta = \arctan\left(\frac{\omega}{c\gamma}\right) \tag{3.2}$$

where c is the propagation velocity of the disturbance. Figure 9 shows the inclination

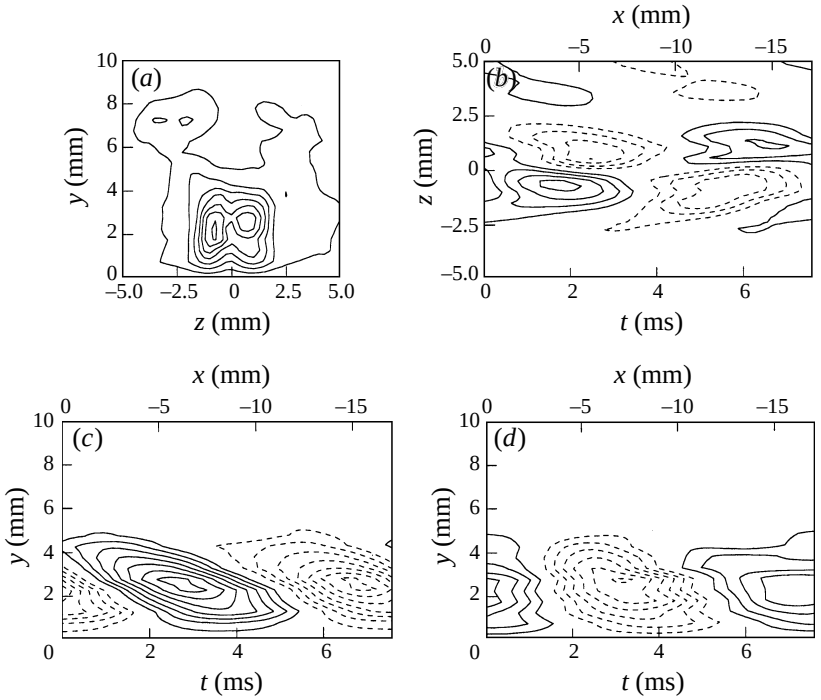

FIGURE 8. Structure of secondary instability at $x = 836$ mm: (*a*) r.m.s. of streamwise velocity, (*b*) velocity disturbance in (z,t)-plane at $y = 3.8$ mm, (*c*) velocity disturbance in (y,t)-plane at $z = -0.5$ mm, (*d*) velocity disturbance in (y,t)-plane at $z = 0.5$ mm. Contour spacing is 1% U_b.

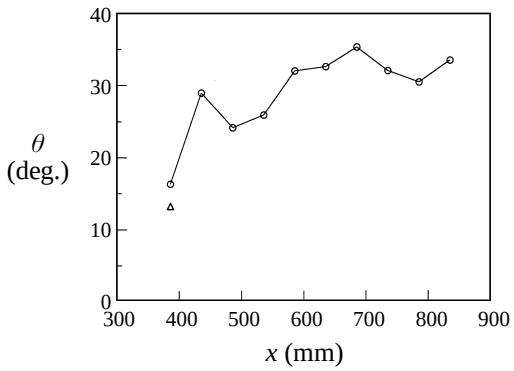

FIGURE 9. Inclination (○) of secondary instability structure in (y,t)-plane. The inclination of the corresponding disturbance without rotation is also plotted (△)

θ at different streamwise positions, and it is increasing in the downstream direction from 16° to 33°.

3.3. *Phase velocity and growth rate*

The propagation velocity of the secondary instability was obtained by measuring the disturbance at two different x-positions ($x = 528$ mm and $x = 536$ mm) located $\Delta x = 8.0$ mm apart in the streamwise direction. Because the secondary disturbance was phase locked with the initial disturbance, it is possible to correlate the signals to get the time shift (Δt) for maximum correlation. The measurements were made

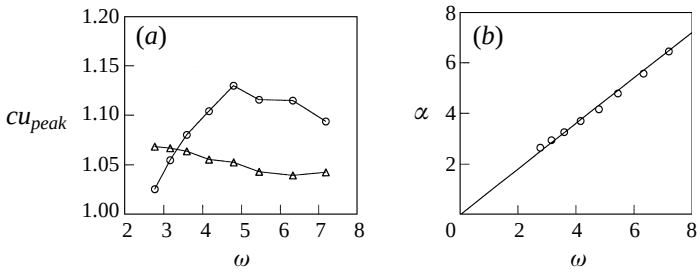

FIGURE 10. Phase velocity and wavelength. (*a*) Comparison between phase speed and streamwise velocity at the peak. ○, phase speed; △, streamwise velocity at the peak. (*b*) ○, streamwise wavenumber α. Slope of line is equal to the mean phase velocity of the different frequencies.

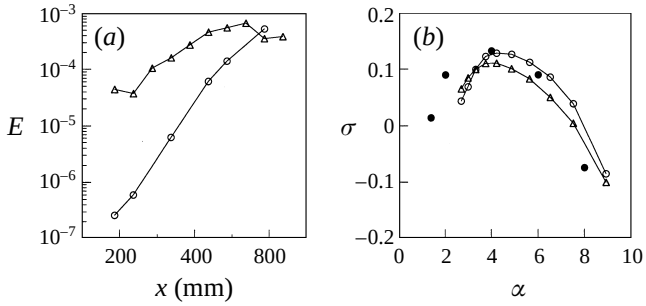

FIGURE 11. Disturbance energy growth and growth rate. (*a*) Energy growth: ○, one speaker forcing; △, two speaker forcing. (*b*) ○, one speaker forcing, growth rate determined from data between $x = 436$ mm and 636 mm; △, two speaker forcing, growth rate determined from data between $x = 436$ mm and 486 mm; ●, data from Finlay (1990).

close to the peak region. The non-dimensional phase velocity was determined as $c = \Delta x/(\Delta t U_b)$. Figure 10(*a*) shows the resulting values of the phase velocity as a function of the disturbance frequency. The streamwise phase velocity is normalized with the bulk velocity and it is seen to be slightly higher. In figure 10(*a*) also the mean velocity at the peak position u_{peak} (normalized with U_b) is plotted. In general the phase velocity is close to both the bulk velocity and streamwise velocity at the peak of the fundamental disturbance. The velocity at the peak is almost constant independent of frequency; however the phase velocity increases with frequency in the low-frequency region and slightly decreases in the high-frequency region. The maximum phase velocity is at $\omega = 4.8$ which also corresponds to the frequency for maximum growth rate, as will be shown later. The phase speeds observed here are in close agreement with those reported by Finlay (1990, see his figure 8) and Yang & Kim (1991), who for the present parameter range obtained values around $1.1U_b$–$1.15U_b$.

The streamwise wavenumber of the disturbance was obtained as $\alpha = \omega/c$ and increases linearly with ω as shown in figure 10(*b*) (due to the almost constant phase speed). At 150 Hz ($\omega = 4.8$) this corresponds to a wavelength of 15 mm.

Figure 11(*a*) shows the streamwise energy growth of the secondary disturbance for two different initial disturbances. In one case two speakers are used as shown in figure 2, and in the other case only one speaker is used. In the one speaker case the disturbance grows exponentially from $x = 436$ mm to 636 mm and then the growth rate decreases slightly downstream. In the two speaker arrangement a higher initial

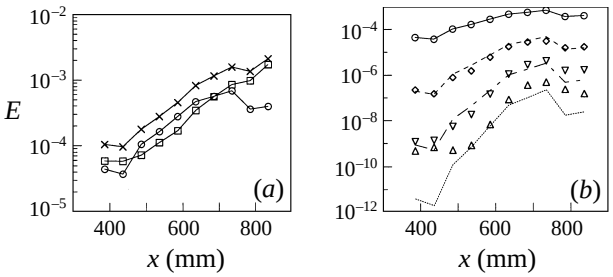

FIGURE 12. Disturbance energy development of various components. (*a*) ×, total; ○, fundamental; □, random, (*b*) ○, $E(F_1)$; ◇, $E(2F_1)$; ▽, $E(3F_1)$; △, $E(4F_1)$; ——— , $E(F_1)$; – – – – , $\sim E^2(F_1)$; –·–·– , $\sim E^3(F_1)$; · · · · · , $\sim E^4(F_1)$.

amplitude was used and the region of linear growth is hence shorter. The growth rate between $x = 436$ mm and 483 mm is close to the growth rate in the one speaker case. Further downstream the growth rate becomes smaller and reaches its maximum at $x = 786$ mm. For an exponentially growing disturbance the amplitude development can be written as

$$A = A_0 \mathrm{e}^{\sigma x/d}$$

where σ can be estimated from the slope in figure 11(*a*) (note that this figure shows the energy growth and the slope is therefore twice the value of σ).

In figure 11(*b*) the growth rates in the linear region for these two initial amplitudes are shown as a function of the streamwise wavenumber α. In both cases the maximum growth rate is at $\alpha = 4.2$ (corresponding to $\omega = 4.8$ or $f = 150$ Hz, which is close to the frequency of the naturally occurring secondary instability). The growth rate is larger than 0.1 in a fairly wide wavenumber range. Also shown in the figure are data from Finlay (1990, see his figure 7) for $Re\,Ro^{1/2} = 174$ and $\beta = 6$. As can be seen good agreement between experiments and numerical simulation is found, especially in the region of maximum growth.

3.4. *Higher modes and nonlinearity*

Figure 12(*a*) shows the energy growth of various components in the streamwise direction. Here the initial disturbance has the same amplitude as in figure 2, i.e. the forcing is of high amplitude. Three curves are shown, namely the overall r.m.s., the r.m.s. of the fundamental frequency and the r.m.s. of the non-coherent or random contribution. The streamwise velocity signals were ensemble-averaged with the phase of the speaker signal as reference. The integrated disturbance energy was used as a measure of its intensity. The total energy of the velocity fluctuation, E_{total}, is defined as

$$E_{total} = \frac{1}{\lambda d} \int_{-\lambda/2}^{\lambda/2} \int_0^d u_{r.m.s.}^2 \,\mathrm{d}y\mathrm{d}z, \tag{3.3}$$

where $u_{r.m.s.}$ is the root-mean-square of the streamwise velocity. We denote the energy at the fundamental frequency F_1 by E_{fund} and the energy associated with the harmonics ($2F_1$, $3F_1$, etc.) by $E_{harm.modes}$, which are determined by summing the contributions from the forcing frequency component and its harmonic modes respectively. The contribution to the energy from the random modes (E_{random}) was estimated as follows:

$$E_{random} = E_{total} - E_{fund} - E_{harm.modes}$$

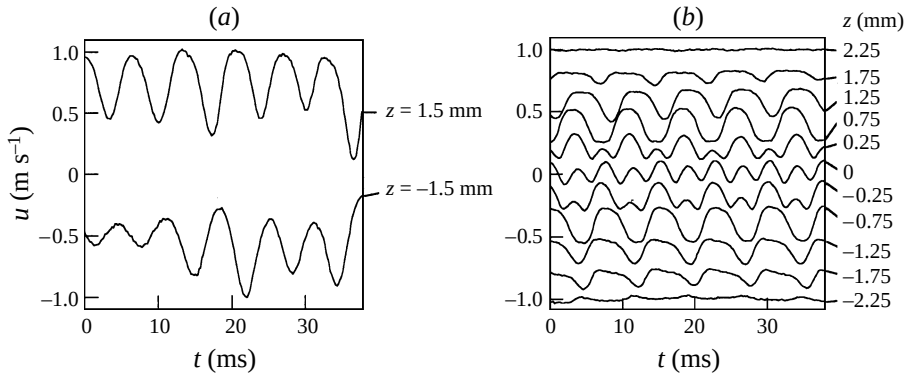

FIGURE 13. Velocity signals. (*a*) Simultaneous velocity signals of natural disturbance obtained with two hot wires separated by 3 mm in spanwise direction at $x = 836$ mm, $y = 2.75$ mm. (*b*) velocity signals with forcing at several spanwise position, at $x = 636$ mm, $y = 3.8$ mm. Velocity reference is arbitrary.

By viewing the spectra it is clear that the high-frequency contribution to the energy is due to the fundamental and its harmonics, whereas E_{random} mainly is related to low frequencies and hence the undulating motion. In figure 12(*a*) the energy of the fundamental is seen to decrease between 386 mm and 436 mm before it starts to grow. Around $x = 736$ mm it saturates and decreases slightly further downstream. The random mode, however, always shows an increase in the streamwise direction. The harmonic modes have a larger growth rate than the fundamental mode (figure 12*b*). The lines shown in the figure are obtained from the growth of the fundamental, and by taking the second, third and fourth power of the fundamental the development of the harmonics can be well estimated (the lines are shifted vertically to obtain the best fit in the linear region). Hence the growth rates of the second, third and fourth modes are two, three and four times as large as the fundamental one, respectively, which is to be expected from a quadratic nonlinear process.

If a natural secondary instability is detected with two hot-wire probes, one at each side of a low-velocity region, one observes that the signals are out of phase as shown in figure 13(*a*). This shows that the secondary instability is a wavy mode. In the forcing case, the out-of-phase signals are clearly shown by the phase locking with the forcing as shown in figure 13(*b*). It is worth noticing that the signals on and close to the spanwise symmetry line clearly show the existence of the first harmonic mode. This result will be further discussed in §4.

As was discussed in connection with figure 12 the signal consists of both coherent and non-coherent parts. The coherent part consists of both the fundamental and its harmonics. Through filtering it is possible to obtain the spatial distribution of the various harmonics as well as of the random contribution. Figure 14(*a–c*) shows the energy distribution in the (y, z)-plane at $x = 436$ mm for the fundamental, the first and second harmonics (figure 14*d,e* will be discussed later). The fundamental has a symmetric distribution with two peaks close to $y = 4$ mm. The peaks of the harmonics are further away from the unstable wall than the fundamental peaks. The first mode has one large peak on the symmetry line, while even modes (fundamental and second) contain two peaks symmetrically located around $z = 0$.

Energy distributions at $x = 636$ mm (figure 15) are similar in terms of two peaks symmetrically in the even harmonic mode cases and one large peak at the centre for

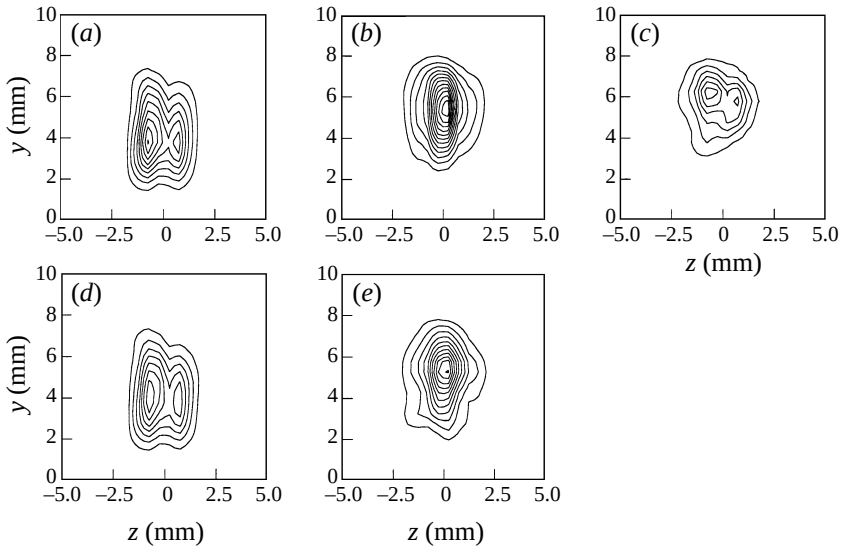

FIGURE 14. Energy distribution of streamwise velocity disturbance at $x = 486$ mm: (*a*) fundamental mode (contour spacing is 0.005% U_b^2), (*b*) first harmonic mode (contour spacing is 0.0001% U_b^2), (*c*) second harmonic mode (contour spacing is 2×10^{-7}% U_b^2), (*d*) estimated fundamental mode (contour spacing is 0.005% U_b^2), (*e*) estimated first harmonic mode (contour spacing is 0.0001% U_b^2).

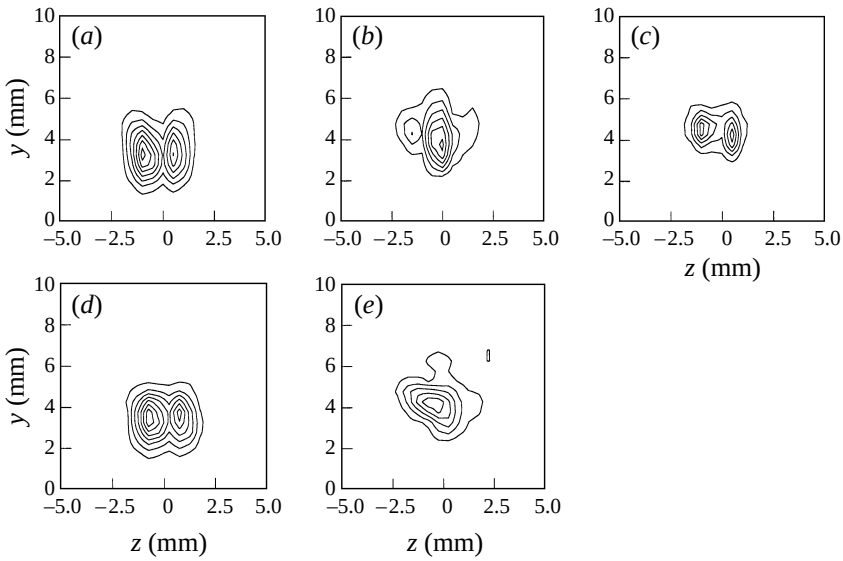

FIGURE 15. Energy distribution of streamwise velocity disturbance at $x = 636$ mm: (*a*) fundamental mode (contour spacing is 0.1% U_b^2), (*b*) first harmonic mode (contour spacing is 0.005% U_b^2), (*c*) second harmonic mode (contour spacing is 0.0005% U_b^2), (*d*) estimated fundamental mode (contour spacing is 0.1% U_b^2), (*e*) estimated first harmonic mode (contour spacing is 0.005% U_b^2).

the first harmonic mode, though the peaks shift towards the unstable wall in all cases and small peaks of the first harmonic mode appear besides the large peak at the centre.

Figure 16 shows the wall-normal position of the centre of energy that corresponds to the peak position. The positions are shifted towards the unstable wall with streamwise

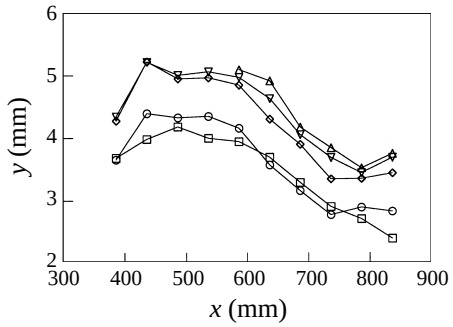

FIGURE 16. Height of centre of energy for $F = 131$ Hz: ○, fundamental; ◇, first harmonic mode; ▽, second harmonic mode; △, third harmonic mode; □, random.

position for all modes except $x = 386$ mm. Though the position of the fundamental mode is slightly higher than the random mode at the growing region between 436 mm and 583 mm, it overlaps with the position of the random mode downstream. The height of the positions of harmonic modes increases with the harmonic order independently of the streamwise position.

3.5. *In-phase disturbance*

It seems clear from the natural disturbance growth that out-of-phase disturbances are more unstable than in-phase disturbances, since this type is the dominant one. Even when in-phase disturbances are forced in the experiment they never become dominant except just downstream of the forcing. For the present conditions the growth rate of the in-phase mode was negative which explains why the natural secondary instability appears as out of phase.

3.6. *Transition to turbulence*

Even with forcing, the random part of the disturbance energy becomes dominant in the downstream part of the channel (see figure 12). This is the first step towards turbulent flow. The flow becomes random through the growth of natural disturbances besides the forced one and their subsequent nonlinear interaction. Figure 17(*a–d*) shows a number of frequency spectra which illustrate various features of this process. In all figures the natural disturbance spectrum for the case of no rotation is also shown at $x = 836$ mm as a reference. As can be seen the natural disturbances are mainly found in the interval 100 to 200 Hz.

Figure 17(*a*) shows the frequency spectra of the natural disturbances at some different downstream positions. In the rotating case it is seen how a rather sharp peak around 150 Hz is growing in the downstream direction from $x = 536$ mm to $x = 686$ mm and that at $x = 836$ mm it has started to broaden. Also, its higher harmonics are clearly seen. A frequency band around 50 Hz is also detected at $x = 536$ mm and 686 mm, which can be explained as modulation between the modes of 150 Hz and 100 Hz. The low-frequency components around 30 Hz increase strongly from $x = 636$ mm to 836 mm. These low-frequency components may stem from modulation of various components between 100 Hz and 200 Hz.

In the case of forcing at $F = 131$ Hz sharp peaks at the forcing frequency and its harmonic modes appear as shown in figure 17(*b*). The modulation between the 131 Hz and 155 Hz peaks (the latter is from the background noise) also gives a sharp peak around 24 Hz.

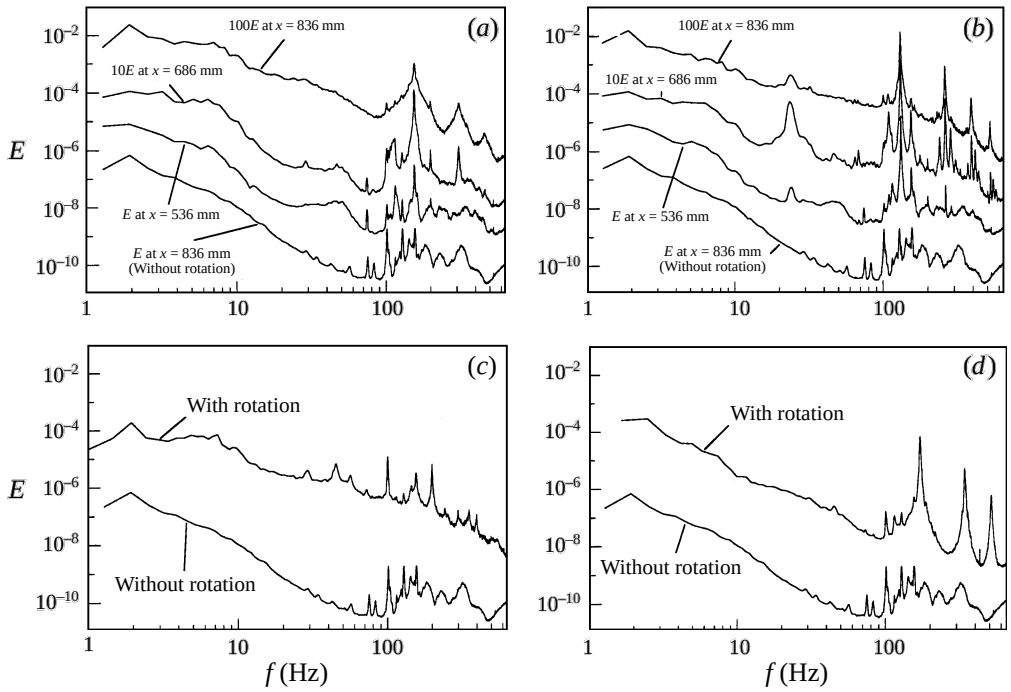

FIGURE 17. Power spectra of the streamwise velocity averaged over the measurement domain for different forcing frequencies at different x-positions, with and without rotation. (a) without forcing, (b) forcing at $F_1 = 131$ Hz, (c) forcing at $F_1 = 100$ Hz, $x = 836$ mm, (d) forcing at $F_1 = 172$ Hz, $x = 836$ mm.

This kind of modulation between peaks of short-wavelength disturbances is also found in cases of 100 Hz forcing (figure 17c) and 172 Hz forcing (figure 17d). A notable result is that energy in the low-frequency region (2 Hz to 50 Hz) in the natural and 131 Hz forcing cases increases between $x = 686$ mm and 836 mm. This energy increase contributes to the large growth of the random motion at $x = 836$ mm seen in figure 12. The transition to turbulent flow stems at least partly from this low-frequency band which gains energy through the modulation process between the short-wavelength secondary instability and background noise.

4. A model of the secondary disturbance

In the previous section it was seen that the velocity signal is dominated by the first harmonic mode at the spanwise centre of the low-velocity region (see figure 13a). Figure 18 explains the mechanism of this phenomenon briefly. Assume that the distribution of the streamwise velocity around a low-velocity region is as in figure 18(a). It is assumed that the secondary instability results in a wavy motion where the streamwise momentum to first order is preserved. If a velocity sensor sensitive to the streamwise velocity is located in the region of high shear it will record a signal which is mainly the fundamental mode (figure 18b). On the other hand when the sensor is located at the centre of the valley as shown in figure 18(c), higher harmonics can be observed (figure 18d).

We propose a model of the secondary flow which is useful to explain some of the observations in this experiment. It can also be used to approximate the normal and spanwise velocity fields associated with the secondary flow.

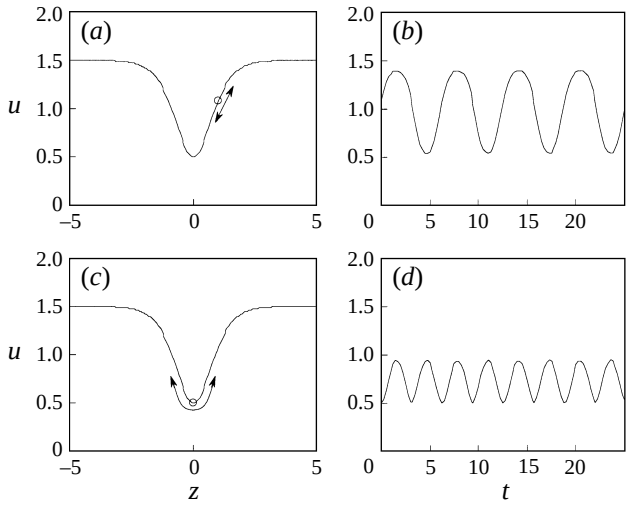

FIGURE 18. Relation between sensor position and velocity signal: (*a*) sensor at point of strong spanwise shear, (*b*) velocity signal showing fundamental frequency for wavy motion, (*c*) sensor at centre of low-velocity region, (*d*) velocity signal showing twice the fundamental frequency for wavy motion. Scales are arbitrary but the same in all cases. The wavy motion is also the same.

If the measured streamwise velocity field is time-averaged we obtain the velocity distribution $\bar{u}(y,z)$. We now assume that the streamwise velocity acts as a passive scalar for the wavy motion. At the position $y = y_0$, $z = z_0$ the streamwise velocity is assumed to be of the form

$$u(t; y_0, z_0) = \bar{u}(\eta, \zeta) \tag{4.1}$$

where

$$\eta = y_0 + \frac{v(t)}{\omega}, \quad \zeta = z_0 + \frac{w(t)}{\omega}.$$

To first approximation the cross-stream velocities of the wavy motion are

$$v = \hat{v}(y,z)\sin(\phi), \quad w = \hat{w}(y,z)\sin(\psi)$$

where

$$\phi = \omega t + \theta_v, \quad \psi = \omega t + \theta_w.$$

This model of the secondary instability motion states that fluid particle trajectories are ellipses when projected on the (y,z)-plane. By assuming that the velocity can be written in the form (4.1) it is possible to obtain values of $\hat{v}$, $\hat{w}$, θ_v, θ_w for each (y,z) pair. This is done through an optimization process in which the four parameters ($\hat{v}$, $\hat{w}$, θ_v, θ_w) are varied in a consistent way and a best fit to the measured time signal is obtained. The optimization process was done by the Simplex search method in the commercial software *Matlab*. This fitting is sensitive to experimental noise, so that the 20×21 measurement points used (including the values at the walls) of the mean streamwise velocity were first smoothed by using six Fourier modes in the spanwise direction and eight Chebychev modes in the normal direction. Figure 19 shows comparisons between measured (u) and fitted ($\hat{u}$) velocity fields in (z,t)-planes at two streamwise positions. As can be seen the agreement is excellent.

Also, the wall-normal velocity v and the spanwise velocity w can be plotted from the distributions of $\hat{v}$ and $\hat{w}$ and are shown in figures 20 and 21. The wall-normal velocity

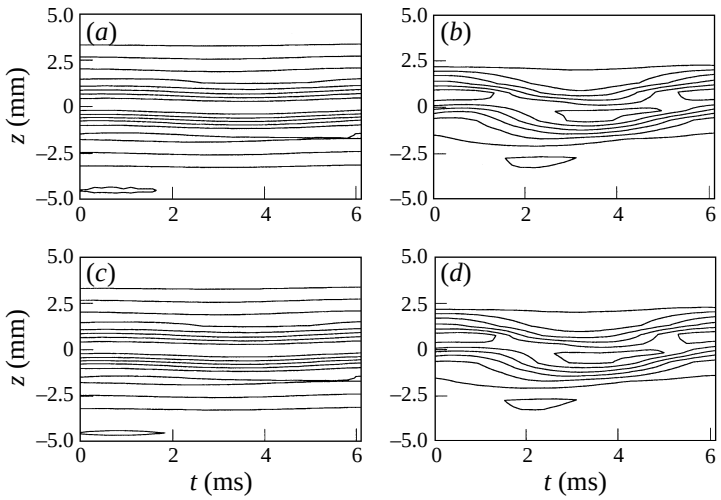

FIGURE 19. Wavy structure and comparison with the fitting at $y = 3.75$ mm. Original experimental data at (*a*) $x = 486$ mm and (*b*) $x = 636$ mm. Fitted data with procedure described in text at (*c*) $x = 486$ mm and (*d*) $x = 636$ mm. Contour spacing is 0.05 U_b.

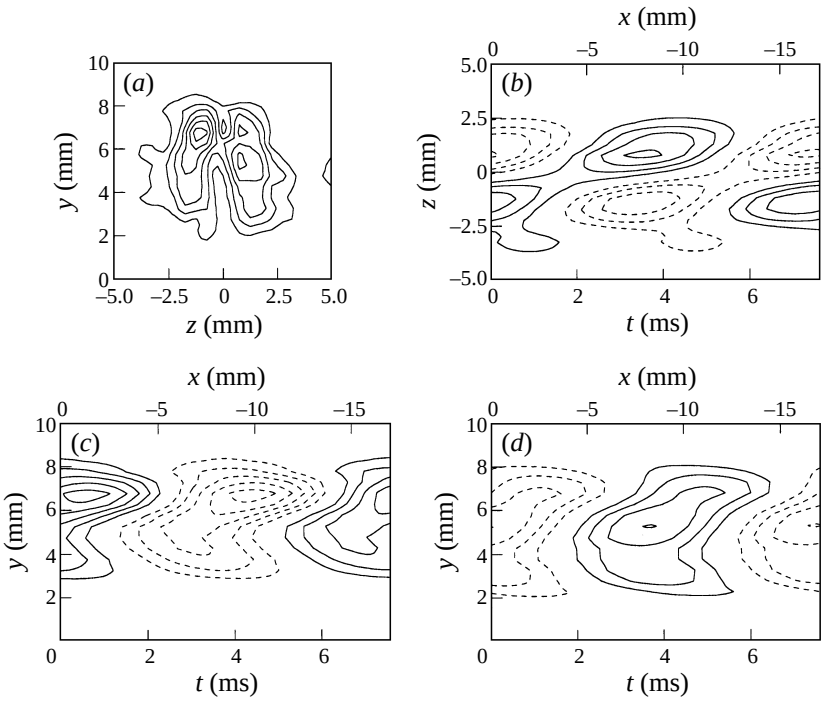

FIGURE 20. The estimated wall-normal disturbance velocity v: (*a*) r.m.s., (*b*) (z,t)-plane at $y = 5.8$ mm, (*c*) (y,t)-plane at $z = -1$ mm, (*d*) (y,t)-plane at $z = 1$ mm. Contour spacing is 0.25% U_b for (*a*) and 0.5% U_b for (*b*), (*c*) and (*d*).

is out of phase like the streamwise velocity shown in figure 6, while the spanwise is symmetric around $z = 0$. Both distributions are concentrated around $y = 6$ mm, and hence they are further from the unstable wall than the streamwise disturbance distribution. The maximum v and w disturbance velocities are about $0.03U_b$. Though

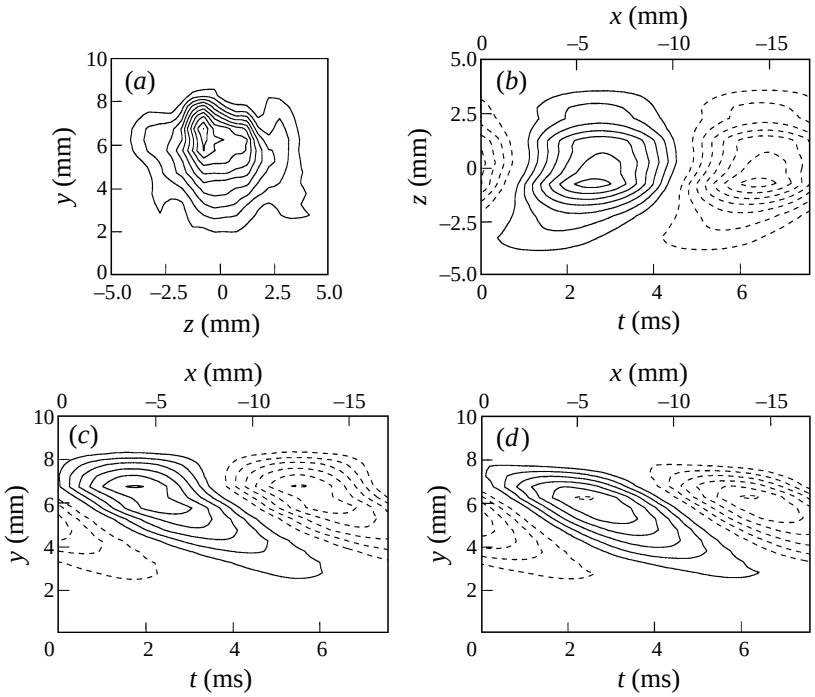

FIGURE 21. The estimated spanwise disturbance velocity w: (*a*) r.m.s., (*b*) (z,t)-plane at $y = 5.8$ mm, (*c*) (y,t)-plane at $z = -1$ mm, (*d*) (y,t)-plane at $z = 1$ mm. Contour spacing is 0.25% U_b for (*a*) and 0.5% U_b for (*b*), (*c*) and (*d*).

(y,t)-planes of v do not show any specific inclination, the structure of w is inclined at about 30° to the wall. This is similar to the inclination of the structure associated with the streamwise velocity (see figure 6).

The physical cross-flow field consists of both the primary and secondary disturbance velocities. For viewing an actual cross-flow field, the cross-flow fluctuations are added to the cross-flow field given by a two-dimensional numerical calculation of the steady saturated basic flow. For the basic flow field the cross-stream velocity components in the normal and spanwise directions reach values of 0.10 and $0.06U_b$, respectively. This means that the cross-flow velocities associated with the twisting motion will affect the cross-flow associated with the primary cross-flow instability significantly. Figure 22 shows the cross-flow at six different times during half of a cycle. The direction of the upwash region is oscillating in the spanwise direction which is also seen in numerical results of Finlay (1990) (in his figure 9, the plot order is opposite because it is a sequence in x and not in t).

If the amplitude of the wavy motion is smaller than the spanwise scale of the profile we can expand the expression for u around the original position in the cross-stream plane (y_0, z_0). We do the expansion up to second order and for each frequency we keep only the lowest-order terms

$$u = \bar{u} + \frac{\hat{v}}{\omega}\sin(\phi)\frac{\partial \bar{u}}{\partial y} + \frac{\hat{w}}{\omega}\sin(\psi)\frac{\partial \bar{u}}{\partial z} - \frac{1}{4}\left[\left(\frac{\hat{v}}{\omega}\right)^2 \cos(2\phi)\frac{\partial^2 \bar{u}}{\partial y^2} + 2\frac{\hat{v}}{\omega}\frac{\hat{w}}{\omega}\cos(\phi+\psi)\frac{\partial^2 \bar{u}}{\partial y \partial z} + \left(\frac{\hat{w}}{\omega}\right)^2 \cos(2\psi)\frac{\partial^2 \bar{u}}{\partial z^2}\right]. \quad (4.2)$$

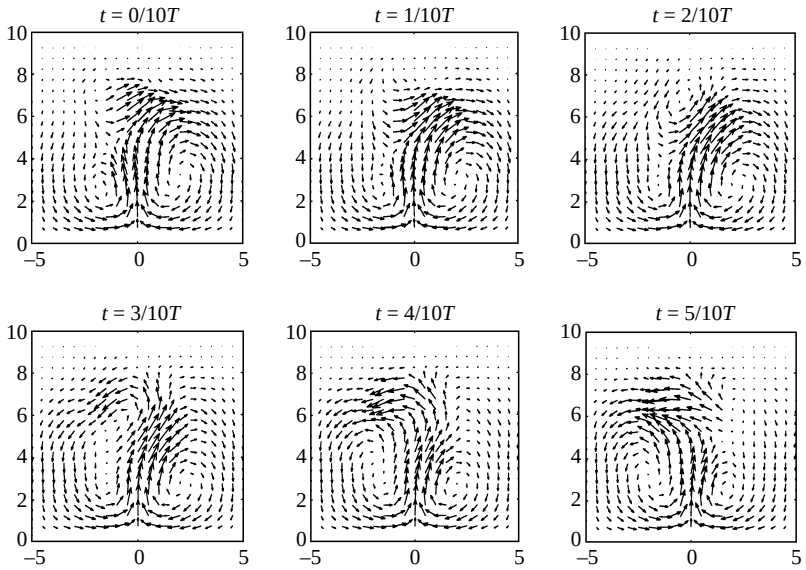

FIGURE 22. Time sequence of the estimated cross-flow velocity distribution at $x = 486$ mm. T is one period of the disturbance at $F_1 = 131$ Hz.

This expansion shows that the first harmonic is related to the second derivative of $\bar{u}$, whereas higher harmonics can be shown to be related to higher derivatives of $\bar{u}$. This expression also shows directly that the growth rate of the higher modes in u should be proportional to the harmonic order. It also shows that the odd harmonics will have a maximum at $z = 0$ (since the even spanwise derivatives of $\bar{u}$ have a maximum at that position). From (4.2) we can also obtain estimates of both the fundamental and the first harmonic of u, since we have obtained values of $\hat{v}$ and $\hat{w}$ (as well as for θ_v and θ_w) previously from the fit of experimental data. Also, higher harmonics are in principle possible to obtain although the measurement data do not everywhere allow accurate determination of the higher derivatives.

In figures 14 and 15 both the directly measured (*a, b*) and estimated distributions (*d, e*) obtained from (4.2) of the fundamental and first harmonic are shown. As can be seen both the spatial distribution, with two peaks for the fundamental and one for the first harmonic, and the amplitudes are well predicted by the model.

5. Summary

The present work maps the development of the twisting type secondary instability towards turbulence in rotating channel flow. The primary instability is in the form of counter-rotating streamwise vortices which are induced by a Coriolis instability whereas the secondary instability consists of high-frequency travelling waves. It is the first extensive experimental study where time-dependent secondary instability is introduced in a controlled way on top of a primary stationary instability. The characteristics of this secondary instability have been determined in detail. The following points summarize the findings.

- Only the sinuous mode was found to be unstable. Even if the varicose mode was triggered, it was damped and the resulting disturbance was sinuous.
- The amplitude distribution of the sinuous mode shows two distinct maxima at

each side of the low-velocity (upwash) region between two vortices. The distribution seems to be related to the spanwise gradient of the mean flow, i.e. its maximum amplitude is found in the region of the spanwise inflection points of the basic flow.

• The phase speed of the disturbance is close to the local velocity at the amplitude maximum, and hence also close to the local velocity in the inflectional region. This together with the measured amplitude distribution strongly suggests that the secondary instability is of inflectional origin.

• The growth rate of the secondary disturbance was determined for various frequencies and it has a clear maximum for $\alpha \approx 4$ ($\omega \approx 5$). This wavelength (frequency) is close to that which is observed for naturally developing flow.

• Higher harmonics of the secondary disturbance have a growth rate which is the harmonic multiple of the growth rate of the fundamental (i.e. first harmonic has twice the growth rate, second harmonic has three times the growth rate etc.)

• Some information on the later stages in the transition process is obtained from frequency spectra of the streamwise velocity signal. It is shown that interaction between various modes gives rise to stochastic low-frequency disturbances which probably is an important ingredient in the transition scenario.

• A theoretical model is described which allows the determination of the cross-stream disturbance flow field under the assumption that fluid particles move in the form of an ellipse during a period of the disturbance. By assuming that the streamwise momentum is carried as a scalar by the disturbance flow field the cross-stream disturbances may be obtained from the measured streamwise velocity. The results show good qualitative correspondence to results from numerical simulations.

• An expansion of the streamwise velocity in terms of the cross-flow disturbance component and derivatives of the mean flow gives the possibility of estimating the higher harmonics. Good agreement for the first harmonic was obtained.

Thanks are due to Marcus Gällstedt who skillfully constructed parts of the experimental equipment. The work was supported by the Swedish National Board for Industrial and Technical Development (NUTEK). The stay at KTH of Dr Matsubara was partly supported by the Göran Gustafsson foundation.

REFERENCES

Aihara, Y. & Koyama, H. 1981 Secondary instability of Görtler vortices: Formation of periodic three-dimensional coherent structure. *Trans. Japan Soc. Aero. Space Sci.* **24**, 78–94.

Alfredsson, P. H. & Persson, H. 1989 Instabilities in channel flow with system rotation. *J. Fluid Mech.* **202**, 543–557.

Bippes, H. & Görtler, H. 1972 Dreidimensionale Störungen in der Grenzschicht an einer konkaven Wand. *Acta Mech.* **14**, 251–267.

Bottaro, A. & Klingmann, B. G. B. 1996 On the linear breakdown of Görtler vortices. *Eur. J. Mech.* B/*Fluids* **15**, 301–330.

Corke, T. C. & Mangano, R. A. 1989 Resonant growth of three-dimensional modes in transitional Blasius boundary layers. *J. Fluid Mech.* **209**, 93–150.

Finlay, W. H. 1990 Transition to oscillatory motion in a rotating channel. *J. Fluid Mech.* **215**, 209–227.

Finlay, W. H. 1992 Transition to turbulence in a rotating channel. *J. Fluid Mech.* **237**, 73–99.

Finlay, W. H., Keller, J. B. & Ferziger, J. H. 1988 Instability and transition in curved channel flow. *J. Fluid Mech.* **194**, 417–456.

Guo, Y. & Finlay, W. H. 1991 Splitting, merging and wavelength selection of vortices in curved and/or rotating channel flow due to Eckhaus instability. *J. Fluid Mech.* **228**, 661–691.

Klebanoff, P. S., Tidstrom, K. D. & Sargent, L. M. 1962 The three-dimensional nature of boundary layer instability *J. Fluid Mech.* **12**, 1–34.

Le Cunff, C. & Bottaro, A. 1993 Linear stability of shear profiles and relation to the secondary instability of Dean flow. *Phys. Fluids* A **5**, 2161–2171.

Lezius, D. K. & Johnston, J. P. 1976 The structure and stability of turbulent boundary layers in rotating channel flow. *J. Fluid Mech.* **77**, 153–175.

Li, F. & Malik, M. R. 1995 Fundamental and subharmonic secondary instabilities of Görtler vortices. *J. Fluid Mech.* **297**, 77–100.

Liu, W. & Domaradzki, J. A. 1993 Direct numerical simulation of transition to turbulence in Görtler flow. *J. Fluid Mech.* **246**, 267–299.

Masuda, S., Hori, D. & Matsubara, M. 1995 Secondary instability associated with streamwise vortices in a rotating boundary layer. In *IUTAM Symp., Laminar-Turbulent Transition* (ed R. Kobayashi), pp. 69–76. Springer.

Matsson, O. J. E. & Alfredsson, P. H. 1990 Curvature and rotation induced instabilities in channel flow. *J. Fluid Mech.* **210**, 537–563.

Matsson, O. J. E. & Alfredsson, P. H. 1992 Experiments on instabilities in curved channel flow. *Phys. Fluids* A **3**, 1666–1676.

Matsson, O. J. E. & Alfredsson, P. H. 1994 The effect of spanwise system rotation on Dean vortices. *J. Fluid Mech.* **274**, 243–265.

Matsubara, M. & Alfredsson, P. H. 1996 Experimental study of heat and momentum transfer in rotating channel flow. *Phys. Fluids* **8**, 2964–2973.

Saric, W. S. 1994 Görtler vortices. *Ann. Rev. Fluid Mech.* **26**, 379–409.

Swearingen, J. D. & Blackwelder, R. F. 1987 The growth and breakdown of streamwise vortices in the presence of a wall. *J. Fluid Mech.* **182**, 255–290.

Tani, I. & Aihara, Y. 1969 Görtler vortices and boundary-layer transition. *Z. Angew Math. Phys.* **20**, 609–618.

Yang, K.-S. & Kim, J. 1991 Numerical investigation of instability and transition in rotating plane Poiseuille flow. *Phys. Fluids* A **3**, 633–641.

Yu, X. & Liu, J. T. C. 1991 The secondary instability in Goertler flow. *Phys. Fluids* A **3**, 1845–1847.